EL SEVIER

Contents lists available at ScienceDirect

Cement and Concrete Research

journal homepage: www.elsevier.com/locate/cemconres



Mineralization dynamics of metakaolin-based alkali-activated cements



Juan Pablo Gevaudan ^a, Kate M. Campbell ^b, Tyler J. Kane ^b, Richard K. Shoemaker ^c, Wil V. Srubar III ^{a,*}

- ^a Department of Civil, Environmental, and Architectural Engineering, University of Colorado Boulder, Boulder, CO, USA
- ^b United States Geological Survey, Boulder, CO, USA
- ^c Department of Chemistry and Biochemistry, University of Colorado Boulder, Boulder, CO, USA

ARTICLE INFO

Article history: Received 16 August 2016 Received in revised form 16 November 2016 Accepted 9 January 2017 Available online 19 January 2017

Keywords:

D. Alkali-activated cement

D. Metakaolin

B. X-ray diffraction

B. Microstructure

Nuclear magnetic resonance

ABSTRACT

This paper investigates the early-age dynamics of mineral formation in metakaolin-based alkali-activated cements. The effects of silica availability and alkali content on mineral formation were investigated *via* X-ray diffraction and solid-state ²⁹Si magic-angle spinning nuclear magnetic resonance spectroscopy at 2, 7, 14, and 28 days. Silica availability was controlled by using either liquid- (immediate) or solid-based (gradual) sodium silicate supplements. Mineral (zeolitic) and amorphous microstructural characteristics were correlated with observed changes in bulk physical properties, namely shrinkage, density, and porosity. Results demonstrate that, while alkali content controls the mineralization in immediately available silica systems, alkali content controls the silica availability in gradually available silica systems. Immediate silica availability generally leads to a more favorable mineral formation as demonstrated by correlated improvements in bulk physical properties.

© 2017 Elsevier Ltd. All rights reserved.

1. Introduction

The long-term durability of alkali-activated cements (AACs), potential alternatives to ordinary portland cement (OPC), depends on the stability of the aluminosilicate system, which is composed of aluminosilicate minerals, mainly zeolites, and an amorphous phase that largely resembles a gel precursor to zeolite formation. It is well known that zeolites are thermodynamically metastable and can restructure into higher-stability zeolites over time. Similarly, the amorphous phase, which is less thermodynamically stable, has exhibited a potential to order into zeolitic minerals [1].

The formation and composition of amorphous phases, which is influenced by soluble silica, alkali content, curing time, and temperature, dictate both the type and rate of potential zeolite formation [2]. Both amorphous and mineral phases influence both short-term material properties (e.g., compressive strength) and long-term durability of AACs [3–6]. Previous studies found that increasing soluble silica content in alkali-activating solutions affects short- and long-term mineral dynamics by retarding zeolite formation [4]. In addition, the presence of soluble silica species has been shown to impact reaction kinetics of aluminosilicate precursors (e.g., metakaolin-MK) that form amorphous phases [7]. For example, AACs with initially higher amorphous contents have exhibited greater increases in compressive strength over time, due

E-mail address: wsrubar@colorado.edu (W.V. Srubar).

to a thermodynamic restructuring into more ordered crystalline phases [3,5].

Most previous studies have utilized pure liquid sodium silicate (NaSi) solutions to provide immediately available silica during alkali activation, while other researchers have investigated the utilization of recycled waste glass to produce NaSi solutions [8,9,10]. Studies implementing waste-glass-derived liquid NaSi solutions in fly ashand slag-based AAC materials found no significant microstructural changes between such systems and those using industrially produced NaSi solutions [11,12]. In 2015, Bobirică et al., [13] studied ground waste glass as a solid NaSi supplement to fly ash- and fly ash/slagbased AACs. In this study, samples that included both liquid and solid NaSi supplements demonstrated improved mechanical properties compared to those that were solely glass-supplemented. While these studies demonstrate the impact of liquid versus solid NaSi supplements on bulk material properties, no studies have mechanistically investigated the effect of silica availability and alkali content on the mineralization dynamics of AACs.

1.1. Scope of work

The purpose of this study was to isolate and investigate the effect of time-dependent silica dissolution and alkali content on (a) early-age mineral formation and (b) impact on permeability in MK-based AACs. Previous work has analyzed complex AAC systems from raw materials with variable chemistries (*e.g.*, fly ash, slag) that likely impact dissolution/precipitation kinetics and final composition of AAC binders [7,2,4, 14–15]. In this work, two chemically pure MK-based systems were

^{*} Corresponding author at: 1111 Engineering Drive, ECOT 441 UCB 428, Boulder, CO 80309. USA.

investigated, namely (1) a system activated with sodium hydroxide (NaOH) and liquid sodium silicate (NaSi) solution (that provides immediate silica availability) and (2) a system activated with NaOH with additions of solid waste sodalime glass (that provides gradual silica availability). Solid waste sodalime glass was used to simulate the effect of adding a calcium-rich, yet homogenously reactive, material to explore its impact on mineral dynamics and porosity, as previous work has done with slag- and fly ash-based AAC systems [3,16–17]. The effect of Na:Si ratio on the time-dependent mineralization dynamics at the nanoscale was explored in both systems using X-ray diffraction (XRD) and solid-state ²⁹Si magic angle spinning nuclear magnetic resonance spectroscopy (MAS-NMR). In addition, observable mineral dynamics were correlated with macroscale changes in bulk material properties, namely shrinkage, density, and permeable porosity.

2. Materials and experimental methods

2.1. Materials

Metakaolin (MK) (MetaMax) was supplied by BASF Chemical Corporation (Georgia USA). Table 1 shows the chemical composition of MK, which was obtained *via* inductively coupled optical emission spectrometry (ICP-OES) using a modified technique developed by [18]. Five milliliter of a 7:3 mixture of hydrochloric acid and hydrofluoric acid is combined with 2 mL of nitric acid and placed in the digestion tubes and heated to 95 °C in a digestion block (HotBlock by Environmental Express) for approximately 2 h. Samples were then cooled and brought up to 50 mL with a 1.5% by weight boric acid solution. The samples were then reheated to 95 °C for about 15 min and cooled for analysis. The samples were diluted $10 \times$ and analyzed with an ARL 3410 + ICP-OES. A blank and three standards, which were made by accurately diluting certified standards, were used for calibration. The raw MK was supplemented either with a reagent-grade sodium silicate (NaSi) solution supplied by Sigma Aldrich or waste soda-lime glass. The chemical composition of the NaSi solution was determined to have a Na:Si weight modulus of 2.5, as obtained via ICP-OES. Clear waste soda-lime glass was collected from a recycling waste stream at the University of Colorado Boulder, soaked in a diluted nitric acid bath (5% acid by volume) for 12 h, and washed thoroughly with Alkanox cleaning agent to remove any acidity and residue. Glass was subsequently ground in mill capsules with clean and well-packed yttrium-stabilized zirconium grinding beads (American Elements) at a rate of 0.2 g/min using a McCrone micronizing mill. A No. 325 sieve was used to ensure a sub-45 µm particle size. The chemical composition of the waste glass was measured with the same protocol as MK and is also shown in Table 1. Reagent-grade NaOH pellets with >97% chemical purity (No. S5881) were supplied by Sigma-Aldrich.

2.2. Experimental methods

2.2.1. AAC sample preparation

In this study, two classes of AACs were prepared with liquid-based NaSi (N) and solid-based, waste-glass-supplemented, NaSi (G) supplements with varying molar concentrations – high (H), medium (M), and low (L) – according to the prescribed mix-design parameters shown in Table 2. In these specific mixture formulations, liquid-to-solid (L:S) ratios were 1.5 mL/g for G-samples and 2.25 mL/g for N-samples to ensure complete reaction during mixing. Constant Si:Al ratio of

Table 1
Chemical composition of MK and waste glass in weight percent.

(wt%)	SiO ₂	Al_2O_3	CaO	SO ₄	Fe ₂ O ₃	K ₂ O	Na ₂ O	P ₂ O ₅
MK	54%	47%	0.1%	0.3%	0.4%	0.1%	0.3%	0.1%
Glass	80%	1.6%	12%	0.6%	0.1%	0.7%	13%	

Table 2Sample classifications and mixture proportions for MK-based alkali-activated cements. Na:Si ratios were varied by controlling the amount of NaOH used in preparation of the alkali-activating solution.

	Constituent materials								
	Solids		Alkali-activatin	Sample parameters					
Mixes	MK (g)	SiO ₂ glass (g)	NaSi (SiO ₂ moles)	NaOH (M)	Si:Al	Na:Si	H ₂ O:Na ₂ O		
NH	60	-	0.57	17	2.0	1.4	10		
NM	60	-	0.57	6	2.0	0.7	19		
NL	60	-	0.57	1	2.0	0.5	30		
GH	60	42.3	_	8	2.0	1.6	12		
GM	60	42.3	_	4	2.0	0.9	23		
GL	60	42.3	-	2	2.0	0.7	36		

2.0 for all samples permitted explicit investigation of the effect of Na:Si ratio on the mineralogical evolution in these two AAC systems.

NaOH solutions of different molar concentrations were prepared for each sample to obtain the specified Na:Si ratios, as seen in Table 2, by dissolving NaOH pellets in deionized water under continuous agitation using a magnetic stir bar. Dissolution was performed in a temperature-controlled cold room (4 °C) to minimize evaporation due to the exothermic nature of NaOH hydration. Once the NaOH solutions were prepared, the corresponding amount of NaSi solution (SiO₂:Na₂O: 2.5) was added and the new solution was left to equilibrate for approximately 2 h in the cold room prior to mixing with N-samples. For the glass-based samples, waste glass was added as a solid silica supplement directly to the MK to prevent any glass dissolution prior to sample preparation.

Solids were mixed with their respective alkali-activating solutions to produce MK-based AACs that were silica-supplemented with glass (G-samples) or liquid NaSi solutions (N-samples). All materials were mixed at room temperature using a Waring PDM112 mixer. The mixing procedure consisted of 1 min of initial mechanical mixing, followed by 1 min of hand mixing to ensure no material was unmixed on the sides of the vessel. Hand mixing was followed by 3 min of additional mechanical mixing to ensure homogeneity.

Paste samples were cast in flat disk molds (diameter 5.2 cm) for Xray diffraction (XRD) and solid-state magic-angle spinning nuclear magnetic resonance (MAS-NMR) spectroscopy and cylindrical molds (diameter 2.7 cm, height 10 cm) for density, shrinkage, and permeable porosity testing. Samples were then cured inside hermetically sealed plastic containers that maintained a 100% constant relative humidity. The constant-humidity chamber was prepared according to ASTM E104 by placing a supersaturated salt solution of sodium phosphate (Sigma Aldrich) inside the plastic containers. The containers were placed inside a Quincy forced-air laboratory oven set to 60 °C. The temperature and humidity in each chamber was recorded using an EL-USB-2-LCD temperature and humidity data logger from Lascar Electronics, respectively. Samples were allowed to cure for 2, 7, 14, and 28 days. The containers were opened for 24 h prior to the day of testing to allow samples to dry at 60 °C. Samples were subsequently submerged in acetone (ACS-certified, 0.2% H₂O, Fisher Scientific) for 15 min to halt hydration and then submerged in anhydrous ethanol (200 proof, 0% H₂O, Decon Labs) for 15 min to halt alkali activation prior to experimental testing [11].

2.2.2. X-ray diffraction (XRD)

To determine mineralogy, flat disk samples were first crushed into a powder with a mortar and pestle. The powder was then prepared for analysis using a modified method based on [19]. First, the powder was homogenized and split into a representative aliquot. 1000 \pm 0.5 mg of the powdered sample was mixed with 250 \pm 0.5 mg of corundum (American Elements) as an internal standard and added to a mill

capsule containing clean, well-packed yttrium-stabilized zirconium grinding beads. The mixture was subsequently ground using a McCrone micronizing mill with 4 mL ethanol for 5 min, generating particle sizes with 95% below 30 μm , measured via Malvern Mastersizer 3000 laser diffraction system. A slurry of the mixture was created by adding approximately 25 mL of ethanol and then dried overnight at 60 °C in a laboratory oven. The sample was then placed into a plastic scintillation vial with three Delrin balls. 500 μL of Vertrel cleaning agent (Miller-Stephenson) was added to the sample to generate aggregates with random particle orientation. The scintillation vial was then mixed for 10 min in a SK-L330 Pro mechanical shaker. Finally, the samples were sieved through a 250 μm mesh and packed into XRD analysis plates.

A Siemens D500 X-ray diffractometer was used to acquire diffraction patterns for all samples. Samples were analyzed from 5 to 65° 20 using Cu K α X-ray radiation with a step size of 0.02° and a dwell time of 2 s per step. Mineralogy was identified using Jade software (MDI, version 9) and the International Centre for Diffraction Data (ICDD) 2003 database. Corundum was used to normalize peak heights between samples and to align diffraction patterns.

2.2.3. Solid-state ²⁹Si magic angle spin-nuclear magnetic resonance spectroscopy (²⁹Si MAS-NMR)

Solid-state ²⁹Si MAS-NMR spectra were acquired using a Varian INOVA 400 spectrometer (magnetic field 9.39 T; sample spinning frequency of 12.1 KHz, and transmitter frequency of 79.50 MHz for ²⁹Si observation). ²⁹Si chemical shifts were determined using the absolute spectrometer frequency, calibrated such that the NMR signal from DSS (trimethylsilyl propane sulfonic acid, sodium salt) appeared at 0.0 ppm. Calibrated chemical shifts were referenced to TMS (Tetramethylsilane) within 1 ppm, resulting in a 5–6 ppm shift upfield to the aluminosilicate NMR signal reference as reported by Klinowski et al. [20]. The accuracy of DSS or TMS referencing was verified via MAS ¹H NMR of DSS by setting the proton to 0.0 ppm and using absolute referencing for the ²⁹Si spectra. Thus, peak shifts using DSS and TMS as standards were verified and found to only differ by -1.5 ppm. For the acquisition of ²⁹Si spectra, samples were packed into 4 mm zirconia rotors sealed at either end with Teflon end plugs, and spun at 12.2 kHz in a Varian probe equipped with a 4 mm MAS spinning module designed and manufactured by Revolution NMR, LLC (Fort Collins, CO). The spectra were acquired over 1024 scans using a pulse recycle delay of 5 s, a pulse width of 4.5 μ s, pulse angle of $\pi/2$, and an acquisition time of 20 ms. Each spectrum took on average approximately 90 min to acquire. Deconvolution of NMR data was performed using NUTS® software developed by Acorn NMR, Inc. (http://www.acornnmr.com/software/). All specimens were fully dehydrated to ensure that the presence of well-resolved peaks in the spectra presented here indicate ordered silicon environments and not the presence of free soluble silicon components in the pore solution.

2.2.4. Dimensional shrinkage and density

Dimensional shrinkage was calculated as the percent difference in average diameter of samples prior to bulk permeable porosity tests and initial diameter of the cylindrical molds. The diameters and heights of cylindrical samples were measured using calipers. Using the measured volume and weights of samples from the bulk permeable porosity, the density for each sample was calculated.

2.2.5. Bulk permeable porosity

Bulk permeable porosities were measured using a vacuum-method (ASTM C1202). This method was selected due to its proven higher efficiency when compared to other laboratory methods of calculating permeable porosity [21]. The standard was modified by utilizing anhydrous ethanol in lieu of water to prevent any further alkali-activation or reaction with water. Cylinder samples were first demolded after the 24-hour drying time. A Milwaukee 6-in diameter angle grinder (9000 rpm) with a 3 M polishing disk was used to grind the bottom

and tops of cylinder samples. Sample volumes were calculated by measuring the diameters and heights using calipers. Additionally, samples were subjected to a vacuum of 508 mm-Hg for 24 h. The saturated surface dry (SSD) weight was recorded using a Mettler Toledo PL 1502E scale after ethanol-vacuum immersion. Samples were then dried at 60 °C for 24 h and their oven-dry (OD) weights were recorded. Bulk permeable porosity was calculated as the difference in SSD mass and OD mass normalized by the density of ethanol (0.803 g/cm³) all divided by the total sample volume.

3. Experimental results and discussion

3.1. Time-dependent mineralogy

Mineralogical data were acquired *via* XRD for all AAC pastes at four different curing ages. Table 3 describes the main aluminosilicate minerals identified in at least one sample with their respective unit geometries, volumes, and densities, as determined by each reference standard. XRD patterns shown in Figs. 1 and 2 explicitly show the presence or absence of those minerals in each N- and G-sample, respectively, at 2, 7, 14, and 28 days.

In general, the N-samples exhibit lower mineral diversity and broader peak patterns, indicating a higher disordered mineral structure and/or smaller effective particle size in comparison to the G-samples. In addition, high alkali content promoted early formation of zeolite mineral phases in both N- and G-systems. For example, Faujasite-Na is formed after 2 days in NH samples (Fig. 1a), whereas NL samples (Fig. 1c) exhibit Faujasite-Na formation after 14 days. Sodium carbonate (natrite, Na₂CO₃, 20: 30.15°, 38.00°, 35.24°) was only present in the diffraction patterns of N-samples, suggesting that the sodium in N-samples is more readily available to react with ambient carbon dioxide.

3.1.1. Time-dependent mineralogy of N-samples

The observed mineral formation process for the NH samples was: Zeolite ZSM-3 + Faujasite-Na \rightarrow Zeolite ZSM-3 + Faujasite-Na + Zeolite P \rightarrow Zeolite ZSM-3 + Faujasite-Na + Zeolite P + Zeolite P1 (Fig. 1a). The observed mineral formation process for the NM samples was: Phillipsite-K \rightarrow Faujasite-Na + Phillipsite-K + Zeolite P1 (Fig. 1b). Phillipsite-K is formed at 14 days, increasing in pattern intensity from day 14 to day 28. At 28 days, Phillipsite-K and Zeolite P1 are present. Both minerals have similar unit densities and volumes. NL samples exhibited sparse mineral formation. The observed mineral formation process of the NL samples was: Faujasite-Na \rightarrow amorphous aluminosilicate (Fig. 1c and see Supplementary material). The unexpected disappearance of Faujasite-Na at 28 days might be due to a complete amorphization of the mineral at high Si:Na ratios, as previously reported in literature [30].

Immediate silica availability coupled with a high sodium-alkali content yield early zeolite mineral formation. NH samples exhibit early Faujasite-Na formation from an early age of 2 days through 28 days. Decreased sodium-alkali content reduces mineral formation and retards Faujasite-Na formation, as seen in NM (Fig. 1b) and NL (Fig. 1c) samples. Faujasite-Na formation might be a result from the mineral stabilization of Zeolite ZSM-3, as previously discussed in literature [22]. Zeolite ZSM-3, a low Si: Al mineral phase, was observed at 2 days in NH samples. The formation of this zeolite may be the result of stabilization of an aluminum-rich gel, as described by Garcia-Lodeiro et al. [31]. Such aluminum-rich phases were expected to develop first, given aluminum's higher affinity for dissolution compared to that of silicon [7]. While Zeolite ZSM-3, a synthetic and relatively unstable zeolite, has been reported to convert to Phillipsite (a more stable phase) [23], no Phillipsite was observed in the NH samples under experimental conditions. Instead, Faujasite-Na is observed to form from Zeolite ZSM-3. Previous literature has characterized this mineral stabilization pathway as a loss in the regularity in the cubo-octahedral layer of Zeolite ZSM-3, resulting in the

Table 3Summary of aluminosilicate minerals of interest found *via* XRD with their corresponding symbols. Mineral shapes, unit volumes, and densities have been obtained using the Jade5 zeolite database reference standard. Symbols correspond to peak identification in Figs. 1 and 2.

Mineral name	Stoichiometry	Si:Al	Symbol	Unit geometry	Unit volume (ų)	Density (g/cm ³)	Reference
Zeolite ZSM-3	Na _{1.88} Al ₂ Si _{2.77} O _{9.48}	1.39	Φ	Hexagonal	13,671	2.60	[22]
Zeolite A ^(a)	Na ₂ Al ₂ Si _{1,71} P _{0,48} O _{8,6} -4,32H ₂ O	~1.0	*	Cubic	1843	2.16	[23]
Zeolite P	Na _{3.6} Al _{3.6} O ₃ Si _{12.4} O ₃₂ —14H ₂ O	3.44	0	Tetragonal	1009	2.13	[24]
Sodalite	$Na_8Al_6Si_6O_{24}(OH)_2(H_2O)_2$	1.00	∇	Cubic	703	2.46	[25]
Phillipsite-K	(K,Na) ₂ (Si,Al) ₈ O ₁₆ —4H ₂ O	1.00		Monoclinic	1017	2.22	[26]
Zeolite P1	$Na_6Al_6Si_{10}O_{32}(H_2O)_{12}$	1.67	†	Tetragonal	1013	2.21	[27]
Faujasite-Na	Na _{1.84} Al ₂ Si ₄ O _{11.92} —7H ₂ O	2.00	+	Cubic	15,550	2.02	[28]
Zeolite 5A ^(b)	NaCaAl ₃ Si ₃ O _{12.28} I _{2.8}	1.00	#	Cubic	1856	3.24	[29]

a XRD pattern corresponds to Zeolite A with partial replacement of Si—O bonds with P—O bonds, no significant framework change is reported in [23].

formation of Faujasite-Na [22]. Thus, Zeolite ZSM-3 may give rise to Faujasite-Na, a more stable, yet less dense, mineral [28].

High mineralization rates may degrade the bulk material properties of AACs, as is evident in the NM samples from 14 to 28 days. All N-samples illustrate that, at early ages $(2-14 \, \text{days})$, increases in alkali content from low (-L) to medium (-M) correspond to relatively little change

in overall crystallinity. At later ages (28 days), however, the proportions of crystalline-to-amorphous intensities (C:A Ratio, presented in the Supplementary Material), in both NL and NM samples differ. More specifically, NL samples exhibit the lowest C:A Ratio of all N-samples at 28 days, whereas NM samples exhibit the highest C:A Ratio of all N-samples. As a result, NM samples have the highest change in C:A Ratio

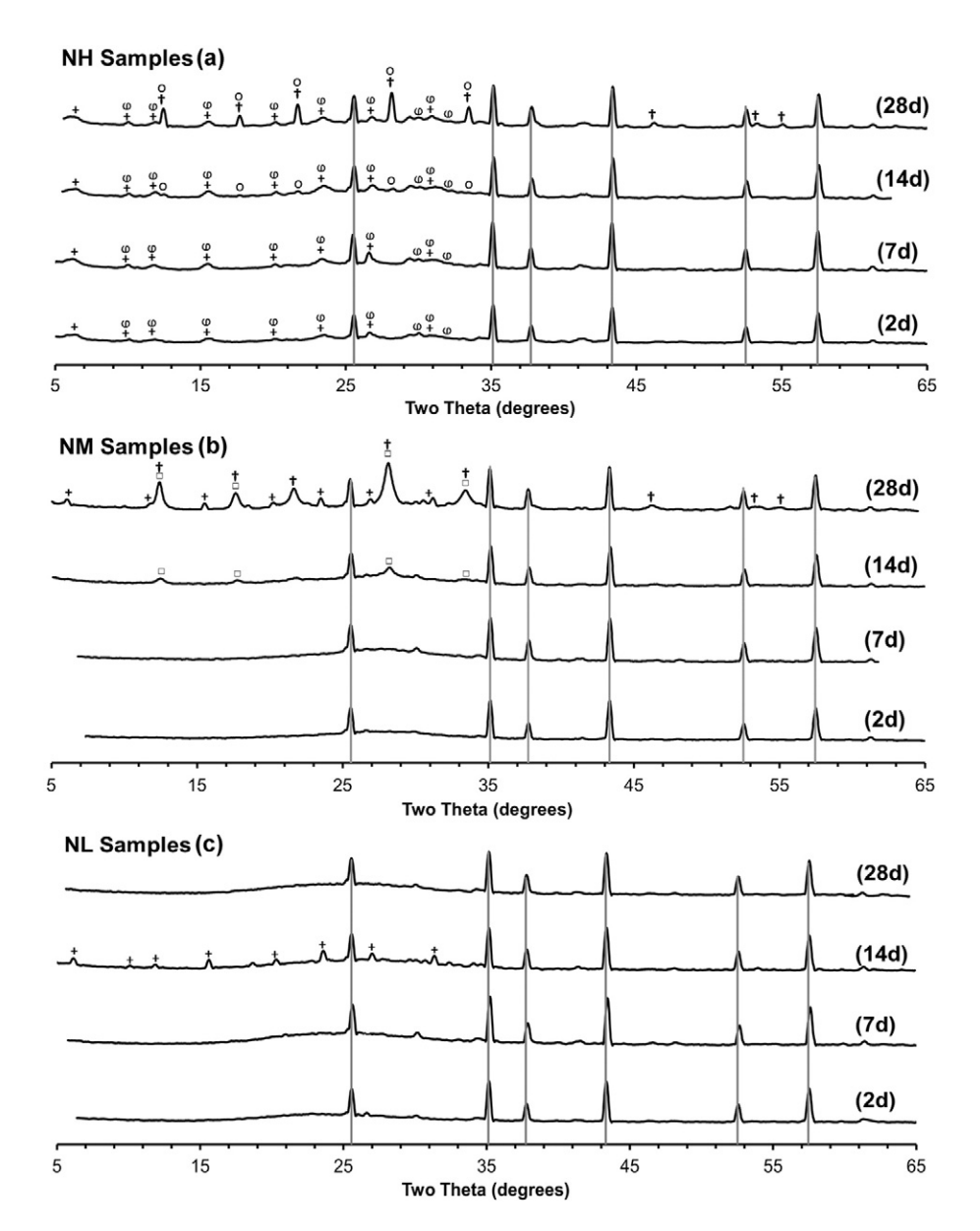


Fig. 1. XRD spectra of NH (a), NM (b), and NL(c) samples at 2, 7, 14, and 28 days. Vertical grey lines correspond to the corundum internal standard. Mineral symbols are defined in Table 3.

b XRD pattern corresponds to Zeolite 5A subjected to iodide absorption; no significant framework changes are reported in [29].

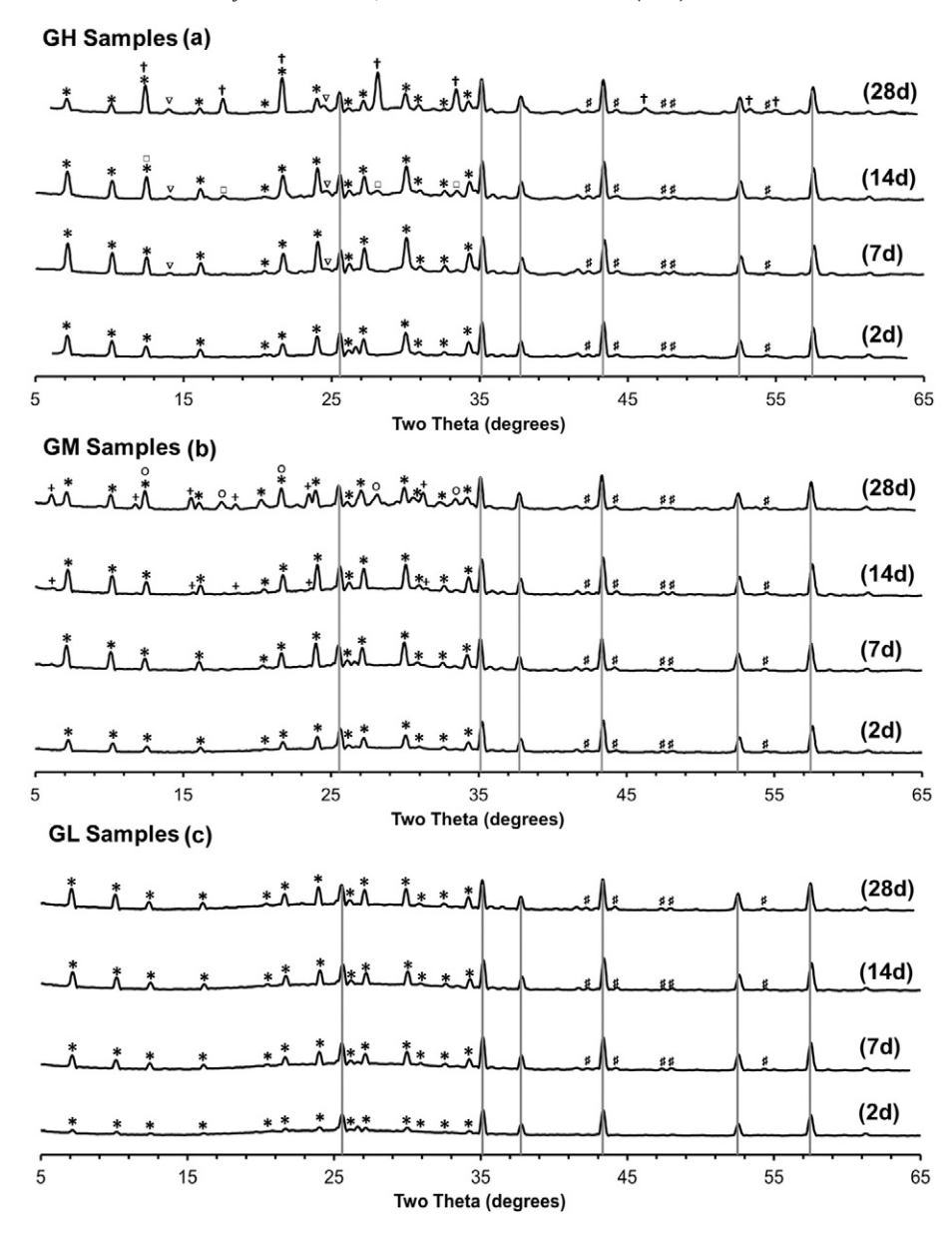


Fig. 2. XRD spectra of GH (a), GM (b), and GL (c) samples at 2,7,14, and 28 days. Vertical grey lines correspond to the corundum internal standard. Mineral symbols are defined in Table 3.

from 14 to 28 days, indicating a rapid crystallization of the sample during that time period. As discussed in Section 3.3, this abrupt change in crystallinity is critical for understanding and, ultimately, controlling bulk material properties of AACs.

3.1.2. Time-dependent mineralogy of G-samples

The observed mineral formation process for the GH samples was: Zeolite A + Zeolite 5A \rightarrow Zeolite A + Sodalite + Zeolite 5A + Phillipsite-K \rightarrow Zeolite A + Zeolite P1 + Sodalite + Zeolite 5A (Fig. 2a). G-samples exhibited rapid crystallization as evident by consistently high C:A Ratios obtained in these samples in comparison to the N-samples. For example, at 7 days, sodalite was formed in GH samples. At 28 days, Zeolite P1 was also present, while Phillipsite-K was only observed at 14 days. The observed mineral formation process for the GM samples was: Zeolite A + Zeolite 5A \rightarrow Zeolite A + Faujasite-Na + Zeolite 5A \rightarrow Zeolite A + Faujasite-Na + Zeolite 7D The intensity of the diffraction pattern for Zeolite A, an aluminumrich mineral, increases from day 2 to 14, while, at 28 days, the

pattern yields to the formation of geometrically distinct Zeolite P. Faujasite-Na is present in GM samples at both 14 and 28 days. While GL samples exhibit sparse mineral formation, the following mineral formation process was observed: Zeolite A \rightarrow Zeolite A + Zeolite 5A, (Fig. 2c).

The results suggest that the gradual incorporation of silica into AAC frameworks (due to slow glass dissolution over time) with high alkali content allows for the transformation of the cubic unit cell of Zeolite A into monoclinic (Phillipsite-K) and later tetrahedral (Zeolite P1) unit cells with successively decreasing dimensions. GH samples at 14 days demonstrate changes in diffraction patterns attributed to decreased Zeolite A and formation of Phillipsite-K. By 28 days, the diffraction pattern of Zeolite A is further reduced and, while Phillipsite-K is no longer observed, Zeolite P1 is present. These results may be indicative of successive solid-solid mineral transformations as suggested by Ostwald's law of successive reactions [32]. The potentially deleterious effect of such solid-solid transformation on bulk porosity is presented in Section 3.3.

The data demonstrate that gradual silica availability (G-samples) and alkali content affects the typology of silicon-rich minerals and

leads to increases in the Si:Al ratio of stabilized minerals over time. In general, incorporation of silicon into silicon-rich minerals can lead to unit cell contractions and higher densities of precursor minerals and amorphous gels. For example, in the GM samples, zeolites that formed from day 7 to day 28 exhibited increases in Si:Al ratio. Zeolite A (Si:Al 1) was present on day 2, while Faujasite-Na (Si:Al 2) and Zeolite P (Si:Al 3.44) are formed by day 28. Increases in Si:Al ratios of zeolites result in mineral phases with higher unit densities and lower unit volumes at later ages compared to those at early ages. Silica availability might reach an optimal level at medium alkali levels. GM samples form silicon-rich Faujasite-Na and Zeolite P. Increasing alkali content hampers the formation of silicon-rich minerals and, instead, forms flexible framework Zeolite P1. Therefore, alkali content, in addition to silica availability, affects mineral variety and typology in gradually available silica systems.

3.1.3. Comparative XRD analysis of N- and G-samples

Fig. 3 summarizes the primary short-term mineral formation, transformation, and stabilization processes for each sample investigated herein. Evidence suggests that the N-samples demonstrate early formation of silicon-rich minerals, while G-samples tend to mineralize faster than N-samples, with most minerals possessing low-silicon contents.

The previously proposed theory of nanocrystalline coexistence within the amorphous phase of AACs [33] can be further supported by the herein observed time-dependent increase in crystallinity in all samples. In the N-samples, pattern intensities increase with time. Aging allows for the gradual stabilization of the aluminosilicate framework *via* thermodynamically favored crystalline mineral formation, as suggested by the observed increase in C:A Ratios, presented in the Supplementary material. The observed time-dependent increase in crystallinity might be due to nucleation and growth of nanocrystals larger than 8 nm, which would make them X-ray visible [34]. As explained by Provis et al. [33], the presence of zeolite nucleation sites dictates the mineralogy present in the microstructure of AACs. Immediate silica availability *via*

liquid NaSi solutions result in low mineral formations due to an increased number of silica-competing zeolite nucleation sites. However, alkali hydroxide-activated cements (AACs without liquid NaSi solutions) produce fewer zeolite nuclei, allowing larger crystal development. These crystals which are unable to pack densely within the binder phase result in a more porous material [33]. In this study, gradually available silica systems (G-samples), examples of alkali hydroxideactivated cements, expectedly exhibit higher degrees of crystallization (higher C:A Ratios), compared to the N-samples. Unexpectedly, however, at medium alkali levels (GM samples), the gradual availability of silica forms silicon-rich Zeolite P (Si:Al ratio of 3.44), a zeolite otherwise only present in NH samples. Also unexpectedly, Faujasite-Na in GM samples is formed earlier, at 14 days, than in NM samples. Therefore, the gradually available silica at this medium alkali content enhances the formation of silicon-rich zeolites. This behavior is unlike the alkali hydroxide-activated cement systems described in [33] as gradually available silica may reduce the silica competition between zeolite nucleation sites, resulting in silicon-rich mineral formation.

Both gradual (G-) and immediate (N-) silica availability at medium and high sodium-alkali contents (Na:Si > 0.5) promote different formation patterns of gismondine-type framework zeolites, Zeolite P and Zeolite P1, at later ages. XRD patterns at 28 days demonstrate that Zeolite P is evident in the GM samples, while Zeolite P1 is present in NM samples. At these same ages, both Zeolite P1 and Zeolite P are present in NH samples, and only Zeolite P1 is present in GH samples. Investigating the effect of alkali content on the formation of these zeolites in N-samples demonstrate that, as the alkali content decreases, only Zeolite P1 is formed. The opposite trend is observed in G-samples, where high alkali contents form Zeolite P1 and medium alkali contents form Zeolite P. Important differences exist between these minerals. For example, Zeolite P1 is flexible and can be readily distorted, while Zeolite Na—P has a higher silica content and the highest possible gismondine-type symmetry [24,27]. Therefore, as alkali content decreases in immediately available (N-) silica systems, favorable formation of flexible gismondine-

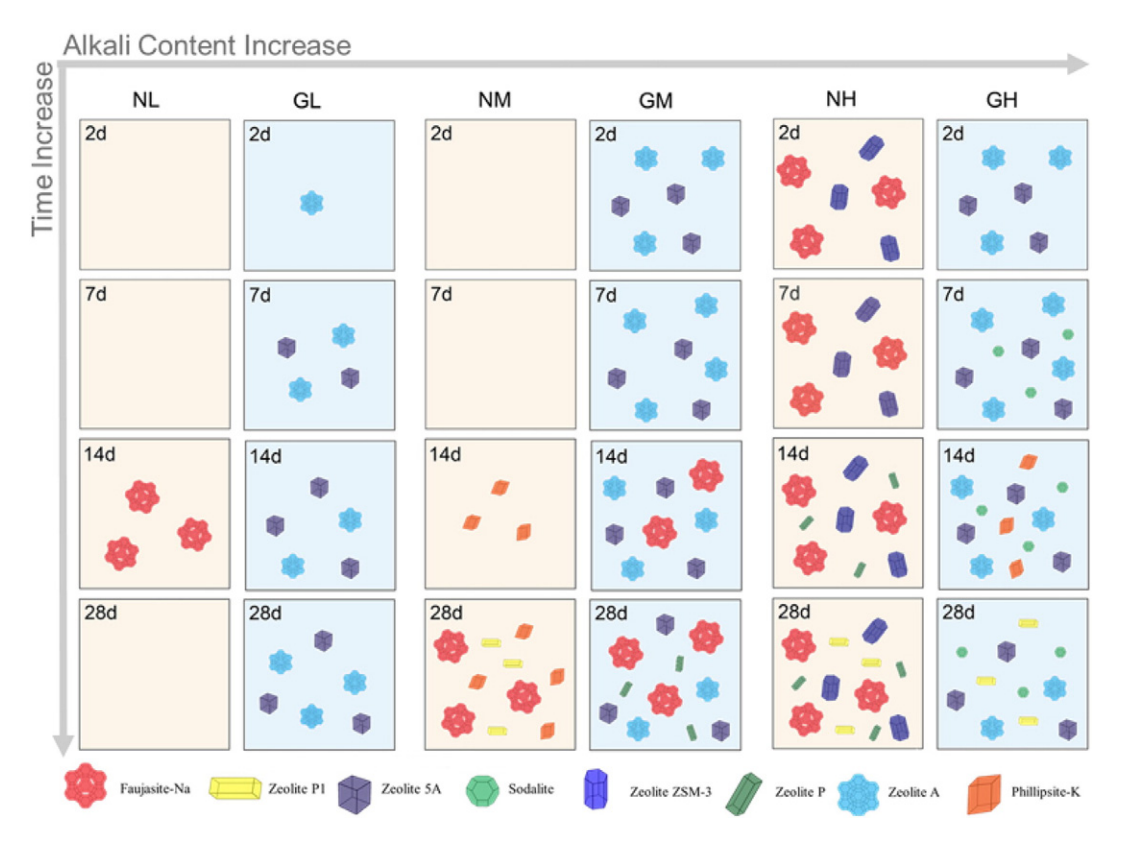


Fig. 3. Mineral dynamics as silica availability and alkali content vary over time based on observed XRD data for all samples. Quantity of minerals depicted is derived from relative intensity of XRD mineral patterns observed for each sample as time progressed.

type framework zeolites occurs, while, in contrast, as alkali content decreases in gradually available (*G*-) silica systems, favorable formation of silicon-rich gismondine-type framework zeolites occurs. As discussed in Section 3.3, different zeolite formation and stabilization pathways induce observable macrostructural changes to bulk physical properties.

3.2. Solid-state ²⁹Si MAS-NMR

3.2.1. ²⁹Si MAS NMR spectroscopy of metakaolin and ground waste glass

The atomic silicon coordination of both raw metakaolin and ground waste glass, which were acquired via ²⁹Si solid-sate MAS-NMR, is shown in Fig. 4. Deconvolution of the spectra was carried out by fitting broad Gaussian curves (fixed linewidths of 4-9 ppm) for silicon-aluminum sites with variable intensities ($Q^4(mAl)$) where m = 0, 1, 2, 3, 4). Peak chemical shifts and full widths at half-height were allowed to vary. The same procedure was maintained for the deconvolution of the glass spectra to account for this amorphous component in G-samples. Expectedly, the NMR spectrum for metakaolin is broad (band width: 100 ppm), indicating a highly disordered environment (Fig. 4a). The main metakaolin peak at -104 ppm corresponds to a predominate Q⁴(1Al) coordination [20], as observed by [35,36,37]. A secondary peak is observed at -91 ppm, which corresponds to $Q^4(3AI)$ atomic coordination [20]. The NMR signal for ground waste glass (Fig. 4b) was also characterized using a reference for alkali silicon glasses from [38, 39]. The main peak at -92 ppm is attributable to Q^3 coordination, as determined for Na₂Ca₂Si₃O₂ glass and seen in [39].

3.2.2. ²⁹Si MAS-NMR of N- and G-samples

Deconvolution of NMR spectra was carried out for all N- and G-samples using a modified methodology presented by Duxson et al. [41], to account for both disordered (amorphous) and higher-order silicon sites. Following their aluminosilicate gel NMR-fitting methodology, broad Gaussian curves with fixed linewidths of 4–9 ppm were fitted for all silicon-aluminum disordered sites with variable intensities ($Q^4(nAl)$). Fitted curves with linewidths <4 ppm were deemed to have higher nanostructural order, exhibiting a higher degree of short and long range order, than disordered sites. Aluminosilicate amorphous material is characterized by a complete distribution of $Q^4(nAl)$, where n

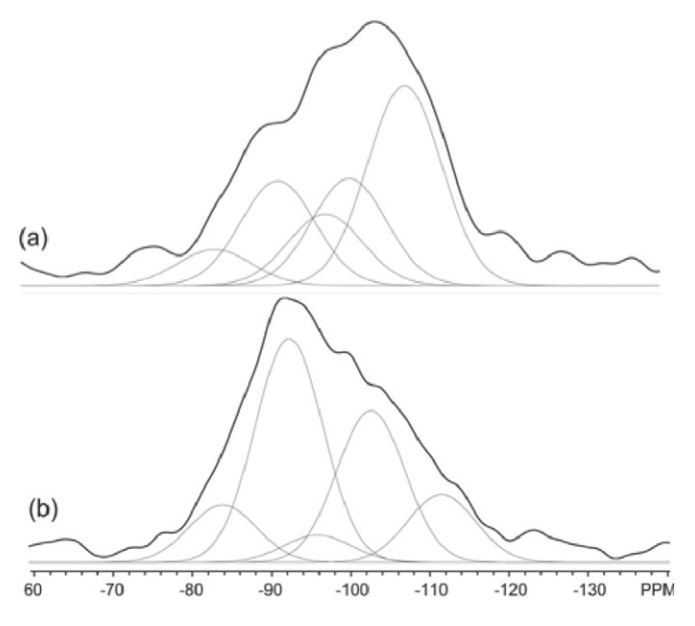


Fig. 4. ²⁹Si solid-state MAS-NMR spectra of both (a) metakaolin and (b) ground waste glass, showing deconvoluted components below each spectrum (Q⁴(0Al): -110 ppm, Q⁴(1Al): -102 ppm, Q⁴(2Al): -96 ppm, Q⁴(3Al): -90 ppm, Q⁴(4Al): -82 ppm) [40]. The main metakaolin peak at -104 ppm corresponds to a predominate Q⁴(1Al) coordination. Note that the main glass peak at -92 ppm coincides with a Q⁴(3Al) coordination in an aluminosilicate system.

varies from 0 to 4 [40]. Disordered peak positions were allowed to vary within the ranges for each $Q^4(nAl)$ coordination, as determined by [20] in a seminal study of aluminosilicate structures. After disordered silicon sites were fitted, clear more ordered silicon sites were fitted with line widths <3–4 ppm and a variable intensity to provide an appropriately summed curve fit. Calculation of internal Si:Al ratios could not be compared with known chemical composition of each sample due to mineral formation affecting the silicon and aluminum contents of the amorphous material. The Si:Al ratio of the amorphous phase was estimated using the following eq. [40]:

where $I_{Si(nAl)}$ is the intensity of each peak in the deconvoluted disordered ²⁹Si spectra for n=0,1,...4. While Si:Al ratio is only appropriate to describe the amorphous material content, it is known that mineral formation or creation of large quantities of Si(0Al) will affect this ratio.

Both MK and glass precursors are consumed as a function of time and alkali content as evidenced by decreasing $Q^4(1AI)$ sites within the amorphous phase. The percentages of silicon coordination sites present in the amorphous phases of N- and G-samples at 7, 14, and 28 days are shown in Fig. 5. The data show that increased alkali content enhances dissolution of both MK and glass. Increased alkali content allows for a lower resonance intensity at -100 ppm, which is attributed to the main resonance of unreacted MK [36], as seen in Fig. 4 and 6. N-samples $(0.5 \le \text{Na:Si} \le 0.7)$ decrease in the Q⁴(1Al) component (~100 ppm) of the spectra as alkali content increases, implying that the signal resulting from MK has been largely diminished (Fig. 5). The lower intensity of the Q⁴(1Al) component could be a result of unreacted MK being almost completely consumed during the synthesis or disruption of the network from dissolution processes [42]. Increase in C:A ratios with alkali content further verify that both unreacted and amorphous material are utilized for zeolite formation. Q⁴(1Al) sites are diminished with time from days 7 to 14 in NM and NL samples. This behavior is not observed in NH samples potentially due to a high C:A ratio, see Supplementary material, and early-age mineralization, minimizing the observed decrease in $Q^4(1Al)$ sites (Fig. 5). G-samples $(0.7 \le Na:Si \le 0.9)$ exhibit the similar trend of increasing O⁴(1Al) and C:A ratios as alkali content increases. Similar to the lower resonance intensity at -100 ppm of MK, G-samples experience an additional, but delayed, decrease in the resonance intensity at -92 ppm, attributed to $Q^4(3AI)$ sites of the AAC and Q^3 sites of glass, see Fig. 4. As seen in Fig. 6, GM and GL samples reduce the resonances at -92 ppm at later ages of 14 and 28 days. The lower intensity of the region could be a result from a gradual dissolution process of glass at later ages due to lower alkali contents. Lower alkali contents are suspected to achieve lower pH levels in the synthesis of AAC pastes,

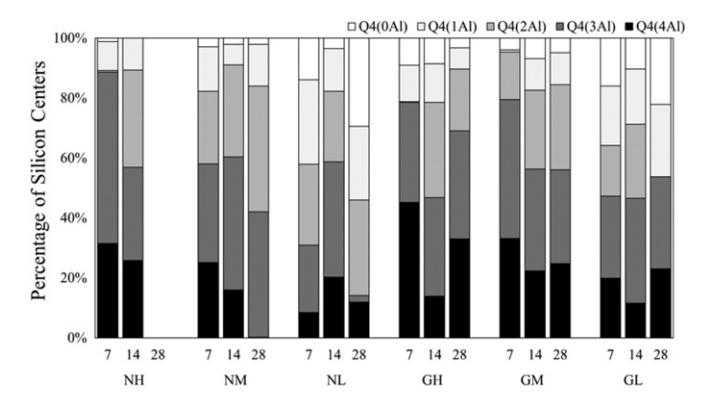


Fig. 5. Fraction of silicon sites present in the amorphous phase as $Q^4(4Al)$, $Q^4(3Al)$, $Q^4(2Al)$, and $Q^4(1Al)$ for all samples as time varies: 7, 14 and 28 days. NH at 28 days is not presented as no amorphous phase was appropriately fitted according to the described methodology.

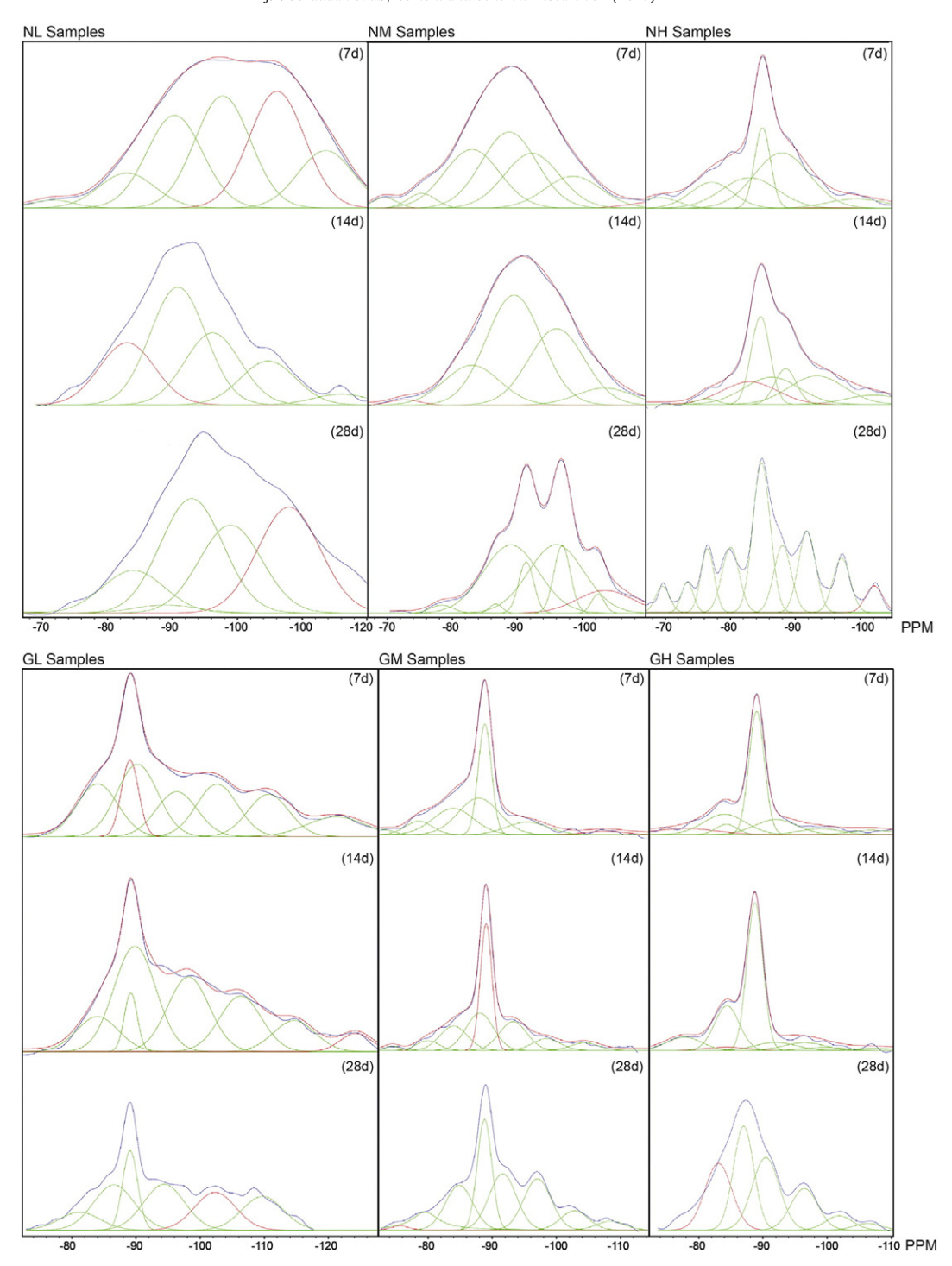


Fig. 6. 29 Si MAS-NMR spectra for the N- and G-samples with deconvolution for each component shown. Deconvolution line total fitted on raw spectra is shown for each sample. Silicon chemical shifts correspond to: $Q^4(0Al)$: -110 ppm, $Q^4(1Al)$: -102 ppm, $Q^4(2Al)$: -96 ppm, $Q^4(3Al)$: -90 ppm, $Q^4(4Al)$: -82 ppm [40].

which would decrease the dissolution process of the glass. Thus, the glass dissolution of GM and GL samples is controlled by a temperature-dependent dissolution of silica. This behavior is not observed in GH samples potentially due to a high C:A ratio, see Supplementary material, and early-age mineralization, minimizing the observed decrease in $Q^4(3Al)$ sites, see Fig. 5.

The propensity for mineralization in AACs, which depends on alkali content, is likely initiated by an increase in aluminum-rich sites, $Q^4(4Al)$ and $Q^4(3Al)$, serving as nucleation sites which subsequently allow for mineral precipitation, yielding a silicon-rich amorphous binder. NH and NM samples increase in silicon incorporation (decrease of

 $Q^4(4Al)$ sites) as the sample ages and silicon-rich minerals form due to unit cell structural changes of formed minerals, as discussed in XRD Section 3.1.1. High alkali content in the absence of available silica likely allows for the unit cell structural changes necessary for the formation of silicon-rich minerals. The high crystallization of NM (see Supplementary material) and decrease in $Q^4(4Al)$ sites form silicon-rich minerals at a Na:Si ratio of 0.6. Creation of silicon-rich minerals is also observed for GM samples likely due to an optimal silica availability at medium alkali levels. GM samples exhibit a similar process of forming silicon-rich minerals *via* consumption of $Q^4(3Al)$ sites, see Fig. 5. Increased mineralization consumes the amorphous phase of AACs, which affects the

proportions of silicon sites reported in Fig. 5. Consumption of aluminum-rich Q⁴(3Al) sites at 28 days in GM samples corresponds to a slight increased proportion of Q⁴(4Al) sites in the amorphous phase. In contrast, GH samples do not exhibit the same trend most likely because (a) the glass NMR signal or (b) the solid-to-solid zeolite transformations obscure the discernment of a real trend in silicon sites. This trend is also not observed for NL and GL samples, because the low alkali content negatively affects the propensity for mineralization. NL samples exhibit low mineralization and a disappearance of silicon-rich minerals after an increase in silicon content of the amorphous phase. Contrastingly, the GL samples exhibit steady mineralization at later ages (14 and 28 days) that corresponds with an increase in Q⁴(4Al) sites. The high content of Q⁴(4Al) sites at 28 days could indicate an increase in nucleation sites resulting in further mineralization if it were tested at later ages. Overall, these results suggest that the creation of silicon-rich minerals is dependent not necessarily on a high Si:Al ratio of the sample, but rather on the aluminum incorporation in the amorphous phase, indicating a propensity for mineralization in AACs.

3.2.3. Disordered and ordered ²⁹Si atomic site distribution in N samples

The presence of higher-order silicon sites is indicated for all N-samples in Table 4, along with the corresponding total deconvolution for all Si(nAl) sites. ^{29}Si spectra of N-samples were, to a large degree, characteristically disordered. The increases of higher order silicon sites as both time and alkali content increase are consistent with observed XRD data for these samples (see Fig. 3). Deshielding of the silicon NMR signal is observed at high alkali contents from 7 days with more increases of Q^4(4Al) and Q^4(3Al) sites than medium and low alkali content samples (NH > NM > NL). Similarly, more ordered silicon sites follow a similar trend with ordered Q^4(4Al) being the only ordered atomic arrangement in the NH sample. This opposite trend is supported by low alkali samples, which have a higher proportion of shielded silicon sites, Q^4(2Al), Q^4(1Al), and Q^4(0Al) (NL > NM > NH), as shown in Fig. 5.

As time progresses, higher silicon magnetic shielding is observed in disordered atomic arrangements of NH and NM samples, see Fig. 6 and Table 4. While both samples decrease in $Q^4(4AI)$ content, higher alkali samples experience shifts to lower resonance frequencies ($Q^4(2,1AI)$) to a greater degree than medium alkali samples ($Q^4(3,2AI)$). As a result there is a greater proportion of Si-O-Si bonds in the amorphous content of the NH at 14 days. The increase of silicon in an aluminosilicate framework decreases its thermodynamic stability, which leads to an

Sample	Age	Qn	Si(4Al)	Si(3Al)	Si(2Al)	Si(1Al)	Si(0Al)	Si:Al
NH	7 day	18%	37% ^(a)	38%	0%	6%	1%	1.30
	14 day	2% ^(a)	39% ^(a)	31% ^(a)	21%	7%	0%	1.47
	28 day	29% ^(a)	28% ^(b)	13% ^(b)	15% ^(b)	10% ^(b)	5% ^(b)	1.49
NM	7 day	5%	24%	31% ^(c)	23%	14%	3%	1.52
	14 day	1%	16%	44% ^(c)	30%	7%	2%	1.51
	28 day	2%	1% ^(a)	40% ^(a)	43% ^(a)	13% ^(a)	2%	1.79
NL	7 day	1%	8%	22%	27%	28%	14%	2.18
	14 day	-	20%	38%	24%	14%	3%	1.55
	28 day	-	12%	2%	32%	25%	29%	2.81
GH	7 day	8%	24% ^(a)	59% ^(a)	0%	5%	4%	1.36
	14 day	9%	25% ^(a)	55% ^(a)	6%	3%	2%	1.73
	28 day	-	52% ^(a)	26%	15%	5%	2%	1.39
GM	7 day	9% ^(a)	21%	58% ^(a)	10%	0%	2%	1.32
	14 day	5% ^(a)	14%	52% ^(a)	17%	7%	4%	1.57
	28 day	11% ^(a)	17%	43% ^(a)	19%	7%	3%	1.54
GL	7 day	-	16%	32% ^(a)	14%	16%	22%	1.86
	14 day	-	10%	37% ^(a)	22%	17%	13%	1.83
	28 day	-	24% ^(a)	38% ^(a)	0%	20%	18%	1.93

a Silicon ordered coordination present.

increased propensity to form zeolites of higher thermodynamic stability [32]. This propensity is affirmed by the observed increase in C:A Ratios and formation of silicon-rich minerals, yielding a silicon-rich amorphous phase, as previously discussed.

Limitations of NMR deconvolution of aluminosilicate gels are evident in samples that have varying degrees of mineralization or incorporation of unreacted material. For example, NMR spectra of medium alkali content samples demonstrate a broad peak at Q⁴(3Al) (8 ppm line width at half maximum), suggesting a disordered environment, see Fig. 6. Such a large line width cannot be confidently deconvoluted using a Gaussian distribution and be classified as a completely disordered atomic environment. While the Duxson et al. [41] NMR deconvolution methodology might seem applicable, XRD data reveal the presence of Phillipsite-K. Due to probable eclipse of ordered signals within disordered signals, this seemingly amorphous system is, in actuality, a composite system of both mineral and amorphous content. Therefore, the results from this study affirm that this methodology is currently limited only to systems of gel aluminosilicates with no significant mineral formation. Further evidence is provided by NL samples, whose respective disordered sites shift toward higher silicon contents. This shift occurs in tandem with the development of silicon-rich minerals (Faujasite-Na) at 14 days as identified by XRD. However, the highly disordered arrangement of NL samples has not allowed for the clear distinction of more ordered peak within the NMR spectra. In addition, the current methodology has not been appropriated to differentiate between unreacted/reacted components of AACs. Instead, the methodology explored herein was employed to better account for more ordered silicon sites as evidenced by mineral formation by XRD.

NH samples at 28 days were characterized by a well-resolved signal peak (2.5 ppm line width at half maximum), which limited the analysis of an amorphous phase, see Fig. 6. Deshielding of silicon's magnetic resonances is observable in NH samples as seen by an increase in Q⁴(4Al) sites and Q_n sites (see Table 4). The increase of higher order $Q^4(4Al)$ sites in the amorphous phase may be indicative of an increase in the mineralization propensity of the cement formation of silicon-rich mineral formation due to aluminum inclusion into a higher order amorphous phase. This hypothesis requires further evidence to be proven. Furthermore, Q_n sites correspond to silicon monomers, dimers, and trimers [43]. The occurrence of this deshielding is most significant in NH samples and thus, it is potentially attributable to high alkali content present in the system or silicon sites at the gel surface, further supporting the assertion of mineralization yielding a silicon-rich amorphous phase. As discussed in Duxson et al. [41], this deshielding might be due to the effects of high alkali content or the high energy penalty associated with the possible formation of Al—O—Al bonds.

3.2.4. Disordered and ordered ²⁹Si atomic sites distribution in G-samples

The presence of higher-order silicon sites indicated for all G-samples is also shown in Table 4. As previously discussed, in gradually available silica systems, the formation of silicon-rich minerals is largely determined by alkali content, as was evidenced by the silicon-rich minerals only observed in the GM samples. Between 14 and 28 days, GM samples formed silicon-rich Zeolite P and Faujasite-Na at high crystallization rates, as determined by the abrupt changes in C:A Ratios in that timeframe, which was accompanied by minimal changes to the distribution of Q⁴(mAl) sites in the amorphous phase between 14 and 28 days (see Fig. 5). This result is expected, given that the creation of Faujasite-Na and other silica rich minerals partly consumes Q⁴(4Al) and Q⁴(3Al) sites of the amorphous phase, as previously discussed. This behavior is also observed in GH samples, which exhibited a decrease in silicon-rich atomic sites, namely Q⁴(2Al), as the amorphous and mineral phases (Zeolite A and Phillipsite-K) are consumed in the formation of Zeolite P1, another silicon-rich mineral, at 28 days. This result is important as higher alkali contents (Na:Si ~1.0) demonstrate a highly dynamic amorphous and crystalline phase than lower alkali contents (Na:Si ~0.5) in samples with gradual silica availability. As alkali

^b Silicon ordered signal fitted with fixed linewidth (2.5 ppm) and ppm shifts.

^c Peaks of high intensity, yet broad linewidth (8 ppm), relating to ordered silicon coordination

content decreases, the silicon content of the more ordered and disordered silicon sites increase from 14 to 28 days. For example, GH samples have a higher content of $Q^4(4Al)$ sites, while GM and GL retain a higher content of $Q^4(3Al)$ sites (see Fig. 5 and Table 4). As a result, gradually available silica slows the solid-solid transformation of the amorphous phase into crystalline zeolites.

As previously discussed, the GM samples were the only samples to form Faujasite-Na and also the only G-samples to exhibit an ordered Q_n formation. The highly deshielded Q_n sites are potentially associated with the formation of silicon-rich zeolites, such as Faujasite-Na, as also seen in the NH samples and, to a lesser extent, the NM samples. This trend is however not observed in NL samples at 14 days, which could be due to an eclipsing of the major disordered silicon sites over those ordered or complete amorphization of Faujasite-Na minerals.

3.3. Bulk physical properties

3.3.1. Density and dimensional shrinkage

The densities and dimensional shrinkages of the N- and G-samples are shown below in Table 5. High density and shrinkage values were achieved either via formation of Faujasite-Na at steady rates or formation of a prominent amorphous phase. NH samples, for example, which demonstrate early formation of Faujasite-Na (see Fig. 3) and with a gradual increase in C:A Ratio from 7 to 28 days, also exhibited the highest density of all samples. In contrast, NL samples, which demonstrated no mineral formation at 28 days and low C:A ratios (see Fig. 3), exhibited the second-highest density and the highest shrinkage at 28 days, which can be attributed to its prominent amorphous phase, see Table 5. The high shrinkage observed is possibly caused by a greater content of silicon-rich phases, which have a greater water content and is suspected to allow greater thermal-shrinkage of the samples and densification [44]. ²⁹Si NMR analysis proves that NL samples have a siliconrich amorphous phase $(Q^4(0AI), Q^4(1AI))$, which exhibit a high density value, see Fig. 5.

Low density and shrinkage values were achieved via rapid and increased formation of minerals. The rapid crystallization of NM samples from 14 to 28 days, as indicated by an increase in C:A Ratio, exhibit the lowest dimensional shrinkage (2%) and a low density. In general, G-samples exhibit high C:A Ratios, indicating high degrees of mineralization. Analysis of the 29 Si NMR spectra of GL samples reveals that these samples also have a greater content of silicon-rich amorphous phase (Q⁴(0Al), Q⁴(1Al)), than their G-sample counterparts. As a result, GL samples exhibit greater shrinkage than GM and GH samples, as previously discussed [44]. However, the shrinkage values are very low compared to N-samples, most probably due to the high crystallization (high C:A Ratios) observed in the G-samples.

3.3.2. Bulk permeable porosity

Fig. 7 shows the permeable porosities obtained at 14 and 28 days for all samples. NH samples exhibited the lowest porosity, while GH exhibits the highest porosity of all samples investigated herein. In general, immediate silica availability allows for the retardation of the rate of

Table 5Density at 28 days and dimensional shrinkage of AAC samples at 7, 14, and 28 days. N/A denotes that no data were able to be collected for this sample due to incomplete curing.

Sample	Density (g/cm ³)	Shrinkage			
		7 Days	14 days	28 days	
NH	1.62	11%	4%	15%	
NM	0.77	N/A	2%	2%	
NL	1.18	16%	11%	16%	
GH	0.72	1%	1%	1%	
GM	0.74	1%	1%	3%	
GL	0.59	4%	2%	3%	

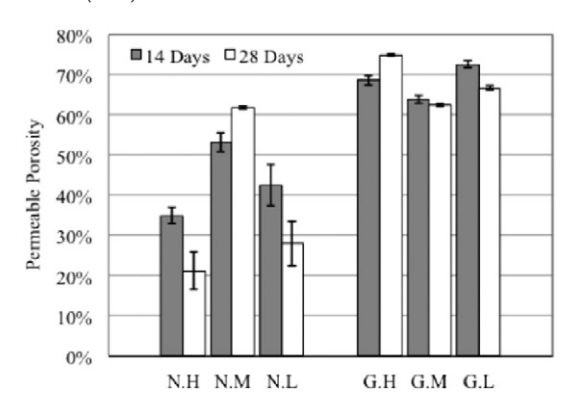


Fig. 7. Bulk permeable porosities of G- and N-samples at 14 and 28 days.

mineral formation and, thus, achieves favorably lower permeable porosities over time in the range of 21%–62%. Gradual silica availability, however, promotes higher crystallization and corresponding increases in permeable porosity, as evidenced by the G-samples.

As discussed, gradual silica availability allows for solid-solid transformations of zeolite minerals, which can lead to higher permeable porosity. For example, in the GH samples, the probable transformation of the cubic unit cell of Zeolite A into a monoclinic (Phillipsite-K) and, later, a tetrahedral (Zeolite P1) unit cell in the GH samples (see Fig. 3) correlates to a 6% increase in permeable porosity. While the mechanism of such solid-solid transformation has not been explicitly studied herein, the observed changes are in agreement with Ostwald's law of successive reactions [32]. The increased porosity of GH samples is expected from the abrupt change in C:A Ratio observed from 14 and 28 days.

The porosity of AACs is thought to be affected by calcium silicate hydrate (CSH) production and mineral dynamics, observed herein, both of which are dependent on alkali type and content. The role of calcium in producing CSH is believed to lower permeability as explored by previous work on slag- and fly ash-based AAC systems [14,15]. These studies are often limited by the variability of the precursors (i.e., fly ash, slag) and their different dissolution/precipitation reactions, alkali content, and resulting mineralogy. Furthermore, the presence of cenospheres in fly ash can be an uncontrolled component, which can increase the porosity of the AAC material. The fly ash used in study [4] was relatively free of calcium-containing phases, but the sodium alkali content was increased by 50% in samples with high replacements of calcium-containing material (slag). These samples exhibited higher permeability with lower calcium contents. However, this change could be due to the significant increase in alkali content due to higher mineralization during curing of these samples. XRD data in studies [4,5] do reveal the presence of Zeolite P1, a zeolitic phase observed in high-alkali samples (NH, GM, NM). Other studies on similar slag, MK, and fly ash AAC systems by [3, 16,17] have demonstrated (a) little reduction in the pore volume fraction of AACs (0.05-0.03) by CSH production or (b) no decrease of total porosity as there is more inclusion of calcium-containing material (i.e., slag). Studies on slag/MK blended systems have demonstrated that decreasing calcium content by 10% decreases permeable voids, yet decreasing it above 20% at higher Si:Al ratios (2.0 and 2.2) increases the percentage of permeable voids. In summary, an optimum amount of calcium replacement may be beneficial to reduce permeable porosity.

The data presented herein (see Fig. 7) illustrate that the permeable porosity of G-samples is higher than those of the N-samples. G-samples contain a 5% solid calcium content, but no CSH was detected in XRD data. However, decreases in permeable porosity are observed for both GM and GL samples. These decreases can be attributed to the specific mineral dynamics observed in these samples, with GL samples having unchanging mineral formations over time and GM forming Faujasite-Na.

Mineralization rate and mineral typology suggest a possible direct influence on the bulk permeable porosities of the AACs investigated herein. The presence of Phillipsite-K and Zeolite P1 (gismondine-type frameworks) in the GH and NM samples coincides with increases in permeable porosity. In addition, the formation of Faujasite-Na and high amorphous contents are known to decrease porosity in AACs [1]. Expectedly, the GM samples experience a slight decrease in porosity that can be attributed to late-age Faujasite-Na formation. The early formation of Faujasite-Na, however, coincides with decreased permeable porosity, as observed for NH, NM, NL, and GM samples.

Data from the NH and NH samples provide evidence that bulk physical properties can be affected by mineral formation and stabilization pathways. Crystallization rates of AAC paste are important for bulk properties. The NH samples exhibit a much more gradual increase in relative C:A phase intensities, yielding a decrease in permeable porosity. Thus, the high alkali content in NH samples allows for higher crystal phase diffraction intensities in proportion to their bulk amorphous signal at an early age, with not much change at later days. Contrastingly, NM samples exhibit a change in C:A ratio of 1.87 from 14 to 28 days (Table SM.1), which relates to a 9% increase in permeable porosity. The steady crystallization behavior most exhibited by NH samples may be critical to minimizing permeable porosity development.

As expected, high shrinkage correlates to a dense material due to a tightening of the matrix, which allows for reduction in porosity. As observed in the data, Table 5 and Fig. 7, NH and NL samples have both the highest shrinkage and density, which correlate to both decreases in porosity from 14 to 28 days. The shrinkage in both samples can be due to loss of water from a silicon-rich amorphous phase composed of Q⁴(0Al) and Q⁴(1Al), as evident in the NL sample (Fig. 5), as discussed in [44]. ²⁹Si NMR deconvolution analysis was limited in the nanostructural analysis of NH samples at 28 days, yet presence of higher-order silicon sites and Qⁿ sites is observed, indicating highly deshielded silicon sites in the amorphous phase. Furthermore, the presence of an amorphous phase can be deduced due to a high shrinkage value as observed in the NL samples.

4. Conclusions

This study isolated and investigated the effects of time-dependent silica dissolution on early-age mineral formation and stabilization in MK-based AACs. The effects of immediate and gradual silica availability and alkali content (Na:Si ratio) on the mineralization dynamics at the nanoscale were explored using XRD and solid-state ²⁹Si MAS-NMR spectroscopy and correlated with macroscale changes in bulk physical properties. Results demonstrate that alkali content affects the mineralization process in immediately available silica systems, while alkali content affects the silica availability in gradually available silica systems. As a consequence, alkali content determines mineral formation in AACs, which, depending on the mineralization rate and type of mineral formed, can impact bulk properties, such as permeable porosity. It is observed that the presence of calcium does not necessarily decrease permeable porosity and that mineral dynamics can play a significant role in the porosity of AACs. Gradual silica availability generally results in increased mineralization and the formation of less favorable minerals.

The time-dependent XRD patterns and NMR spectra, in concert with characterization of bulk physical properties, show that these mineralization and stabilization pathways can have adverse effects on bulk physical properties. For example, the early formation and growth of silicon-rich minerals or the existence of a predominant silicon-rich amorphous phase coincided with reductions in bulk permeable porosity. However, late-age crystallization (amorphous-to-crystalline) and solid-solid (crystalline-to-crystalline) mineralogical transformations, which were observed, both led to increases in porosity. These results demonstrate the importance of understanding and, ultimately, controlling the mineral formation and stabilization dynamics in MK-based AAC systems.

5. Acknowledgments

This research was made possible by the Department of Civil, Environmental, and Architectural Engineering, the College of Engineering and Applied Sciences, and the Sustainable Infrastructure Materials Laboratory (SIM Lab) at the University of Colorado Boulder, with partial support from the National Science Foundation (Award No. CBET-1604457). The collaboration with the United States Geological Survey, the Department of Chemistry, and the Nanocharacterization Laboratory is gratefully acknowledged. In addition, the donation of metakaolin from BASF is appreciated. This work represents the views of the authors and not necessarily those of the University of Colorado Boulder. Any use of trade, firm, or product names was for descriptive purposes only and does not imply endorsement by the U.S. government.

Appendix A. Supplementary data

Supplementary data to this article can be found online at http://dx.doi.org/10.1016/j.cemconres.2017.01.001.

References

- A. Palomo, M.T.T. Blanco-Varela, M.L.L. Granizo, F. Puertas, T. Vazquez, M.W.W. Grutzeck, Chemical stability of cementitious materials based on metakaolin, Cem. Concr. Res. 29 (7) (1999) 997–1004.
- [2] M. Criado, A. Fernández-Jiménez, A. Palomo, Alkali activation of fly ash: effect of the SiO₂/Na₂O ratio. Part I: FTIR study, Microporous Mesoporous Mater. 106 (2007) 180–191
- [3] J.L. Provis, R.J. Myers, C.E. White, V. Rose, J.S.J. Van Deventer, X-ray microtomography shows pore structure and tortuosity in alkali-activated binders, Cem. Concr. Res. 42 (6) (2012) 855–864.
- [4] M. Criado, A. Fernandez-Jimenez, A.G. de la Torre, M.A.G. Aranda, A. Palomo, An XRD study of the effect of the SiO₂/Na₂O ratio on the alkali activation of fly ash, Cem. Concr. Res. 37 (2007) 671–679.
- [5] A. Palomo, S. Alonso, A. Fernandez-Jiménez, Alkaline activation of fly ashes: NMR study of the reaction products, J. Am. Ceram. Soc. 87 (6) (2004) 1141–1145.
- [6] M. Criado, A. Fernández-Jiménez, A. Palomo, Alkali activation of fly ash. Part III: effect of curing conditions on reaction and its graphical description, Fuel 89 (11) (2010) 3185–3192.
- [7] M. Criado, A. Fernández-Jiménez, A. Palomo, I. Sobrados, J. Sanz, Effect of the SiO₂/ Na₂O ratio on the alkali activation of fly ash. Part II: 29Si MAS-NMR survey, Microporous Mesoporous Mater. 109 (2008) 525–534.
- [8] M. Keawthun, S. Krachodnok, A. Chaisena, Conversion of Waste Glasses Into Sodium Silicate Solutions, vol. 12, no. 1, 2014 83–91.
- [9] M. Torres-Carrasco, J.G. Palomo, F. Puertas, et al., Mater. Constr. 64 (314) (2014).
- [10] L.K. Turner, F.G. Collins, Carbon dioxide equivalent (CO₂-e) emissions: a comparison between geopolymer and OPC cement concrete, Constr. Build. Mater. 43 (Jun. 2013) 125–130.
- [11] M. Torres-Carrasco, F. Puertas, Waste glass in the geopolymer preparation. Mechanical and microstructural characterisation, J. Clean. Prod. 90 (2015) 397–408.
- [12] F. Puertas, M. Torres-Carrasco, Use of glass waste as an activator in the preparation of alkali-activated slag. Mechanical strength and paste characterisation, Cem. Concr. Res. 57 (2014) 95–104.
- [13] C. Bobirică, J.-H. Shim, J.-H. Pyeon, J.-Y. Park, Influence of waste glass on the microstructure and strength of inorganic polymers, Ceram. Int. 41 (10) (2015) 13638–13649.
- [14] I. Ismail, S.A. Bernal, J.L. Provis, R. San Nicolas, D.G. Brice, A.R. Kilcullen, S. Hamdan, J.S.J. Van Deventer, Influence of fly ash on the water and chloride permeability of alkali-activated slag mortars and concretes, Constr. Build. Mater. 48 (2013) 1187–1201.
- [15] I. Ismail, S.A. Bernal, J.L. Provis, R. San Nicolas, S. Hamdan, J.S.J. Van Deventer, Modification of phase evolution in alkali-activated blast furnace slag by the incorporation of fly ash, Cem. Concr. Compos. 45 (2014) 125–135.
- [16] S.A. Bernal, R. Mejia de Gutierrez, J.L. Provis, Engineering and durability properties of concretes based on alkali-activated granulated blast furnace slag/metakaolin blends, Constr. Build. Mater. 33 (2012) 99–108.
- [17] R.R. Lloyd, J.L. Provis, K.J. Smeaton, J.S.J. van Deventer, Spatial distribution of pores in fly ash-based inorganic polymer gels visualised by Wood's metal intrusion, Microporous Mesoporous Mater. 126 (1–2) (2009) 32–39.
- [18] R.F. Farrell, S.A. Matthes, A.J. Mackie, A Simple, Low-cost Method for the Dissolution of Metal Mineral Samples in Plastic Pressure Vessels, 1980.
- [19] D.D. Eberl, User Guide to RockJock A Program for Determining Quantitative Mineralogy from X-ray Diffraction Data, 2003.
- [20] J. Klinowski, Nuclear magnetic resonance studies of zeolites, Prog. NMR Spectrosc. 16 (C) (1984) 237–309.
- 21] M. Safiuddin, N. Hearn, Comparison of ASTM saturation techniques for measuring the permeable porosity of concrete, Cem. Concr. Res. 35 (5) (2005) 1008–1013.
- [22] M. Shubaeva, S. Izmailova, I. Karetina, S. Khoshchev, Synthesis and some adsorption properties of ZSM-3 Zeolite, Kinet. Catal. 33 (1992) 191.

- [23] E. Flanigen, R. Grose, Phosphorous substitution in zeolite frameworks, Adv. Chem. 101 (1971) 76–101.
- [24] U. Hakkansson, L. Faelth, S. Hansen, Structure of high-silica variety of zeolite-Na P, Acta Crystallogr. 46C (1990) 1363–1364.
- [25] I. Hassan, H.D. Grundy, Structure of basic sodalite, Acta Crystallogr. 39C (1983)
- [26] J.E.G. Hernandez, J.S.N. del Pino, M.M.G. Martin, F.H. Reguera, J.A.R. Losada, Zeolites in pyroclastic deposits in southeastern Tenerife (Canary Islands), Clay Clay Miner. 41 (5) (1993) 521–526.
- [27] Baerlocher and Meier, Crystal-Structure of Synthetic Zeolite Na-P1, an isotype of Gismondine, Z. Krist. 135 (1972) 339–354.
 [28] R.M. Barrer, J.W. Baynham, F.W. Bultitude, W.M. Meier, Low-temperature crystal
- [28] R.M. Barrer, J.W. Baynham, F.W. Bultitude, W.M. Meier, Low-temperature crystal growth of aluminosilicates, and some gallium and germanium analogues, Hydrothermal Chem. Silic. (1959).
- [29] K. Seff, D.P. Shoemaker, The structures of zeolite sorption complexes. I. The structures of dehydrated zeolite 5 A and its iodine sorption complex, Acta Crystallogr. 22 (2) (1967) 162–170.
- [30] H. Rahier, W. Simons, B. Van Mele, M. Biesemans, Low-temperature synthesized aluminosilicate glasses Part III influence of the composition of the silicate solution on production, structure and properties, J. Mater. Sci. 32 (9) (1997) 2237–2247.
- [31] I. Garcia-Lodeiro, A. Fernández-Jimenez, P. Pena, A. Palomo, Alkaline activation of synthetic aluminosilicate glass, Ceram. Int. 40 (4) (2014) 5547–5558.
- [32] M.E. Davis, R.F. Lobo, Zeolite and molecular sieve synthesis, Chem. Mater. 4 (4) (1992) 756–768.
- [33] J.L. Provis, G.C. Lukey, J.S.J. Van Deventer, Do geopolymers actually contain nanocrystalline zeolites? A reexamination of existing results, Chem. Mater. 17 (12) (2005) 3075–3085.
- [34] P.A. Jacobs, E.G. Derouane, J. Weitkamp, Evidence for X-ray-amorphous zeolites, J. Chem. Soc. Chem. Commun. (1981) 591–593.

- [35] J. Rocha, J. Klinowski, Solid-state NMR studies of the structure and reactivity of metakaolinite, Angew. Chem. Int. Ed. Engl. 29 (5) (1990) 553–554.
- [36] T.T. Tran, S.A. Bernal, J. Skibsted, Characterization of the network structure of alkaliactivated aluminosilicate binders by single- and double-resonance 29Si[27AI] MAS NMR Experiments, 10th International Congress for Applied Mineralogy, 193, 2012. pp. 1–16.
- [37] J.L. Provis, P. Duxson, G.C. Lukey, J.S.J. Van Deventer, Statistical thermodynamic model for Si/Al ordering in amorphous aluminosilicates, Chem. Mater. 17 (11) (2005) 2976–2986.
- [38] D. Freude, J. Karger, NMR techniques, in: F. Schüth, K.S.W. Sing, J. Weitkamp (Eds.), Handbook of Porous Solids, Wiley-VCH, Weinheim, 2002.
- [39] J. Schneider, V.R. Mastelaro, H. Panepucci, E.D. Zanotto, 29Si MAS-NMR studies of Qn structural units in metasilicate glasses and their nucleating ability, J. Non-Cryst. Solids 273 (2000) 8–18.
- [40] G. Engelhardt, D. Michel, High-resolution Solid-state NMR of Silicates and Zeolites, 1987.
- [41] P. Duxson, J.L. Provis, G.C. Lukey, F. Separovic, J.S.J. Van Deventer, ²⁹Si NMR study of structural ordering in aluminosilicate geopolymer gels, Langmuir 21 (2005) 3028–3036
- [42] K.J.D. MacKENZIE, I.W.M. BROWN, R.H. MEINHOLD, M.E. BOWDEN, Outstanding problems in the kaolinite-Mullite reaction sequence investigated by 29Si and 27Al solid-state nuclear magnetic resonance: I, metakaolinite, J. Am. Ceram. Soc. 68 (6) (1985) 293–297.
- [43] J. Davidovits, Geopolymer Chemistry and Applications, third ed. Institut Geopolymere, Saint-Quentin, 2011.
- [44] P. Duxson, G.C. Lukey, J.S.J. van Deventer, Nanostructural design of multifunctional geopolymeric materials, Advances in Ceramic Matrix Composites XI proceedings of the 107th Annual Meeting of the American Ceramic Society 2012, pp. 203–214.